


## Quaternary MgSiN<sub>2</sub>-GaN alloy semiconductors for deep UV applications

Ozan Dernek<sup>✉\*</sup> and Walter R. L. Lambrecht<sup>†</sup>

Department of Physics, Case Western Reserve University, 10900 Euclid Avenue, Cleveland, Ohio 44106-7079, USA

 (Received 2 August 2022; revised 16 October 2022; accepted 23 November 2022; published 14 December 2022)

Ultrawide direct band gap semiconductors hold great promise for deep ultraviolet optoelectronic applications. Here we evaluate the potential of MgSiN<sub>2</sub>-GaN alloys for this purpose. Although MgSiN<sub>2</sub> itself has an indirect gap  $\sim 0.4$  eV below its direct gap of  $\sim 6.5$  eV, its different sign lattice mismatch from GaN in two different basal plane directions could avoid the tensile strain which limits Al<sub>x</sub>Ga<sub>1-x</sub>N on GaN for high  $x$ . Two octet-rule-preserving structures (with space groups  $Pmn2_1$  and  $P1n1$ ) of a 50% alloy of MgSiN<sub>2</sub> and GaN are investigated and are both found to have gaps larger than 4.75 eV using quasiparticle self-consistent *GW* calculations. Both are nearly direct gap in the sense that the indirect gap is less than 0.1 eV lower than the direct gap. Their mixing energies are positive yet small, with values of 8 (31) meV/atom for  $Pmn2_1$  ( $P1n1$ ), indicating only a small driving force toward phase separation.

DOI: [10.1103/PhysRevB.106.235122](https://doi.org/10.1103/PhysRevB.106.235122)

### I. INTRODUCTION

Compact light sources in the deep UV, in particular UV-B and UV-C with wavelengths shorter than 315 and 280 nm, respectively, would have a large impact in science and technology [1]. Light-emitting diodes in this range could fulfill this demand but require new semiconductor materials with efficient doping and band gaps  $E_g > 4$  eV. The current prevailing approach toward this goal is to develop Al<sub>x</sub>Ga<sub>1-x</sub>N alloys, which form a continuous alloy system with a wurtzite structure and end point band gaps of 3.6 eV (GaN) and 6.3 eV (AlN) [2–6]. However, high Al content alloys suffer from a number of challenges: (1) epitaxial growth on GaN substrates results in tensile strain, which tends to develop cracks, (2)  $n$ -type doping with Si leads to a distorted  $DX$  center with a deep level and hence inefficient doping, (3)  $p$ -type doping is even more problematic, and (4) the inverted crystal field splitting of AlN leads to predominantly transverse magnetic (TM) light emission from the basal plane surface [7,8]. Here we propose alloys of MgSiN<sub>2</sub> and GaN as an alternative to overcome at least some of these problems.

Heterovalent ternary semiconductors of the type II-IV-N<sub>2</sub> using group II and group IV element pairs as a replacement for the group III element in III-N nitrides have gained significant interest in recent years [9–11]. These materials have a wurtzite derived structure, which ideally consists of a fully ordered orthorhombic superlattice of wurtzite with space group 33 ( $Pbn_1$  in the setting with  $a_o \approx 2a_w$ ,  $b_o \approx \sqrt{3}a_w$ ,  $c_o = c_w$ , where  $a_w$  and  $c_w$  are the wurtzite and  $a_o$ ,  $b_o$ , and  $c_o$  are the orthorhombic lattice constants, and  $Pna2_1$  if  $a_o$  and  $b_o$  are reversed). They add significant flexibility to the chemical materials design space because one has a choice of II = Be, Mg, Zn, Cd and IV = Si, Ge, Sn. Furthermore, a certain degree of polytypic

disorder with space group 26 ( $Pmc2_1$ ) which also satisfies the octet rule [12] or the presence of exchange defects II<sub>IV</sub> and IV<sub>II</sub> can be tolerated and allows for some disorder tuning of the gap [13–16].

The design flexibility is further enhanced by considering mixed II-IV-N<sub>2</sub> with III-N alloy systems. Recently, the ZnGeN<sub>2</sub>-GaN alloy system was investigated both computationally [17] and experimentally for thin-film growth [18,19]. In particular, it was found that at 50% two octet-rule-preserving structures can be constructed theoretically with space groups  $Pmn2_1$  and  $P1n1$ , of which the former was found to have the lowest total energy. In the  $Pmn2_1$  structure, each N is surrounded by exactly two Ga, one Zn, and one Ge, and the structure can be viewed as half a layer of ZnGeN<sub>2</sub> and half a layer of GaN in the  $b$  direction or a  $[010]_{1/2}$  lattice. Experimentally, alloys at the 50% composition were achieved [18], but their detailed structure and degree of ordering have yet to be confirmed. We point out that a line compound at 50% has been found to exist [20] in the analogous 50% mixed compound of ZnO and LiGaO<sub>2</sub>, which is a mixture of the parent II-VI compound and its ternary I-III-VI<sub>2</sub>.

Here we use this flexibility to search for a semiconductor which is closely lattice matched to GaN and has a gap exceeding 4 eV. From the band gap vs equivalent wurtzite lattice constant diagram in Ref. [10], one can see that MgSiN<sub>2</sub> is lattice matched significantly closer to GaN than AlN and has a predicted direct gap of  $\sim 6.3$ – $6.5$  eV [21,22]. Unfortunately, its indirect gap is about 0.4 eV lower, so it is actually an indirect gap semiconductor, which is undesirable for light emission devices. Upon closer inspection of the lattice match, one should note that the equivalent wurtzite lattice constant in [10] was taken as  $a_o/2$ . However, inspecting the individual orthorhombic lattice constants, there is only a 1.1% mismatch of MgSiN<sub>2</sub> with respect to  $2a_{\text{GaN}}$  in the  $a$  direction but a  $-4.7\%$  mismatch in the  $b$  direction and a  $-4\%$  mismatch in the  $c$  direction. Nonetheless, these can be viewed as acceptable lattice mismatches compared with AlN, which has

\*ozan.dernek@case.edu

†walter.lambrecht@case.edu

−2.4% and −3.9% mismatches in the  $a$  and  $c$  directions compared to GaN. In particular, a compressive strain in the basal plane would be less disadvantageous than a tensile strain, and at least in one basal plane direction, the strain of  $\text{MgSiN}_2$  on GaN would be compressive.

The indirect gap in  $\text{MgSiN}_2$  results from the valence band maximum (VBM) occurring at  $U = (\pi/a, 0, \pi/c)$  in the  $Pbn2_1$  setting of the space group, while the conduction band minimum (CBM) occurs at  $\Gamma = (0, 0, 0)$ . Considering the gap of GaN at  $U$  when it is calculated in an equivalent  $Pbn2_1$  supercell, which lies 1.1 eV below the actual VBM at  $\Gamma$ , and interpolating the direct  $\Gamma$ - $\Gamma$  and indirect  $U$ - $\Gamma$  gaps linearly between  $\text{MgSiN}_2$  and GaN, using a direct (indirect) gap of 3.4 (4.5) eV in GaN and (6.5, 6.1) in  $\text{MgSiN}_2$  [21], one might expect a direct gap up to about 75% and a direct gap of 5.8 eV at that point. Of course, alloy band gaps typically show band gap bowing, and the above also ignores strain effects. Nonetheless, this seemed sufficiently promising to investigate the band gap in a quaternary  $\text{MgSiN}_2$ -GaN system further.

## II. COMPUTATIONAL METHOD

The stability of the 50% alloy is investigated by calculating the cohesive energy vs the isolated atoms, then the enthalpy of formation with respect to the elements in their standard state, and, finally, the mixing energy vs the two end compounds, GaN and  $\text{MgSiN}_2$ . The total energies required for each system are calculated using density functional theory (DFT) within the generalized gradient approximation (GGA) in the Perdew-Burke-Ernzerhof [23] parametrization. The structural parameters, internal positions, and lattice constants were fully relaxed using the QUANTUM ESPRESSO (QE) code [24] within the projector augmented wave method. Subsequently, they were also calculated using the all-electron QUESTAAL code, which implements the full-potential linearized muffin-tin orbital method. In evaluating the total energy differences between different systems, we took care to use exactly the same muffin-tin radii for the atoms in different systems and to use exactly equivalent  $\mathbf{k}$ -point meshes and real-space meshes to maximize systematic error cancellation. All three systems, GaN,  $\text{MgSiN}_2$ , and  $\text{MgSiGa}_2\text{N}_4$ , were calculated in the same 16-atom cell to achieve equal convergence. The cohesive energy calculations use the single-atom energies calculated in large vacuum cells (with spin polarization for Ga, Si, and N) and the stablest form of each species. The cohesive energies of the elements were obtained using both code suites and are compared to experimental values in Table I.

The band structures were calculated using the quasiparticle self-consistent (QS)  $GW$  approach [25,26] implemented in the QUESTAAL code [27]. Here  $GW$  stands for the one-electron Green's function, and  $W$  stands for the screened Coulomb interaction in Hedin's approach [28], which defines the self-energy  $\Sigma = iGW$ . The difference between this non-local and energy-dependent self-energy operator  $\Sigma(\omega)$  and the exchange-correlation potential  $v_{xc}$  is, as usual, calculated within first-order perturbation theory starting from the DFT Kohn-Sham (KS) eigenvalues  $\epsilon_i$  and eigenstates  $\psi_i$ . However, in the QS approach, a new energy-independent, but non-local, potential, expressed by its matrix elements in the basis of KS eigenstates,  $\tilde{\Sigma}_{ij} = \frac{1}{2}\text{Re}[\Sigma_{ij}(\epsilon_i) + \Sigma_{ij}(\epsilon_j)]$ , is evaluated

TABLE I. Cohesive energies of each species calculated by QUESTAAL and QE. The species Ga, Mg, and Si are calculated in their bulk phases, and the  $\text{N}_2$  molecule is calculated in a large vacuum cell. Spin polarization is included for single-atom calculations in QE.

Species	Space group	Cohesive energy (eV/atom)		
		QUESTAL	QE	Expt.
Ga	$Cmce$	−2.69	−2.71	−2.81
Mg	$P6_3/mmc$	−1.50	−1.50	−1.51
Si	$Fd\bar{3}m$	−4.56	−4.62	−4.63
N	$\text{N}_2$	−5.04	−5.18	−4.92

and iterated to convergence. Here  $\text{Re}[\dots]$  means taking the Hermitian part. The eigenvalues thereby become independent of the DFT starting point exchange-correlation choice. They are found to typically somewhat overestimate band gaps because within standard  $GW$  the screening of the Coulomb potential is calculated in the random phase approximation, which underestimates screening. This can be overcome by adding ladder diagrams [29–31], but as a computationally less demanding alternative, it is found that using 80% of  $\tilde{\Sigma}$  and 20% of the DFT exchange-correlation potential usually gives very accurate results for a wide variety of systems [32,33]. We follow this approach here.

The QUESTAAL implementation of the  $GW$  approach uses a mixed interstitial plane wave and product basis set to expand two-point quantities, such as  $W = (1 - vP)^{-1}v$ , with  $v$  being the bare Coulomb interaction and  $P = -iGG$  being the polarization propagator. This is a more efficient basis set than plane waves to represent the screening, and as a result, high-energy states of the KS equation are less crucial to the convergence of the method. The use of an atom-centered basis set allows one to express the self-energy  $\tilde{\Sigma}$  in real space and hence to interpolate for  $\mathbf{k}$  points different from the ones for which  $\Sigma(\mathbf{k}, \omega)$  is calculated. In this way, accurate band dispersions along the symmetry lines and effective masses can be obtained. We tested the convergence of the various parameters entering the  $GW$  calculations, finding a  $3 \times 3 \times 3$   $\mathbf{k}$  mesh, an  $spdf - spd$  basis set including Ga  $3d$  local orbitals, and  $E_{\text{max}}$  above which the self-energy is approximated by an average value to be well converged. Details of the QSGW implementation can be found in Ref. [26].

## III. RESULTS

We here present results for the  $Pmn2_1$  and  $P1n1$  structures, shown in Fig. 1, which were both found to have low energy in the  $\text{ZnGeGa}_2\text{N}_4$  compound at 50% mixing. We start with the structural parameters, given in Table II. We compare the lattice constants with Vegard's average.  $Pmn2_1$  perfectly matches these values. When all the lattice constants and angles between them are relaxed, the  $P1n1$  structure slightly shifts into a monoclinic phase, with the angles between the lattice vectors  $\alpha = \gamma = 90^\circ$  and  $\beta = 90.16^\circ$ . This is consistent with the space group which belongs in the monoclinic crystal system. However, the change in the volume and total energy is negligible. Therefore, we continue to investigate the material in its orthorhombic phase. The  $P1n1$  lattice constant  $a$  falls out of the range set by GaN and  $\text{MgSiN}_2$ , while  $b$  and  $c$

TABLE II. Average bond lengths and relaxed lattice constants for compounds and MgSiGa<sub>2</sub>N<sub>4</sub> structures. Unit cell volumes are compared with Vegard's average of MgSiN<sub>2</sub> and GaN.

	Mg-N (Å)	Ga-N (Å)	Si-N (Å)	<i>a</i> (Å)	<i>b</i> (Å)	<i>c</i> (Å)	Volume (Å <sup>3</sup> )
MgSiN <sub>2</sub>	2.11		1.76	6.504	5.310	5.031	173.75
Expt. <sup>a</sup>	2.09		1.75	6.473	5.272	4.986	170.15
GaN		1.96		6.433	5.571	5.240	187.79
Expt. <sup>b</sup>		1.95		6.378	5.523	5.185	182.65
<i>Pmn</i> 2 <sub>1</sub>	2.06	1.95	1.75	6.467	5.440	5.147	181.07
<i>P1n</i> 1	2.04	1.95	1.75	6.324	5.550	5.159	181.07
Vegard's average				6.469	5.441	5.136	180.75

<sup>a</sup>R. J. Bruls, H. T. Hintzen, R. Metselaar, and C. Loong J. Phys. Chem. Solids 61 1285.

<sup>b</sup>T. Detchprohm, K. Hiramatsu, K. Itoh, I. Akasaki Jpn. J. Appl. Phys. (Japan), vol. 25 (1986), p. L1454-6.

are very close to the GaN lattice constants. Yet the volumes of the two structures are identical. The reduced coordinates for the atoms in *Pmn*2<sub>1</sub> and for *P1n*1 are provided in Appendix. We notice that compared to experimental values, the volume is overestimated by 2.1% for MgSiN<sub>2</sub> and by 2.8% for GaN. We thus also expect an overestimate by a similar amount for the 50% compound. Next, we discuss the total energy results, which allow us to ascertain the stability of the proposed alloy. Table III lists the cohesive energies, enthalpies of formation, and mixing energies, which are all evaluated using both methods. Values obtained using the QE method are given in parentheses. The enthalpies of formation give the energy difference with respect to the elements in their

standard states at room temperature and atmospheric pressure. A negative value indicates stability. A stricter criterion is to evaluate the mixing energy of the alloy with respect to the two separate compounds. These values are positive but quite small. The positive value indicates, as usual for semiconductor alloys, that there exists a miscibility gap and mixing can occur only above a certain temperature where the entropy of mixing makes the Gibbs free energy negative. But once the alloys are formed at the growth temperature, the atomically mixed frozen-in structure is expected to be kinetically stable at lower temperatures. The miscibility gap temperature is directly related to the mixing energy at 50% composition, and a low value indicates a relatively small driving force toward phase segregation and a low mixing temperature. The energy of mixing reported here assumes perfect satisfaction of the octet rule and is thus a lower limit of the mixing enthalpy in a more realistic alloy structure, which may be expected to have a certain degree of disorder, in particular short-range disorder involving local motifs around the N anion deviating from the perfect Ga<sub>2</sub>MgSi by excess Ga, excess Mg, or excess Si. The study of these defects and their energy cost is a topic that needs to be addressed in future research.

Subsequently, we calculated their electronic band structures both in GGA and in the quasiparticle self-consistent *GW* approximations. The results of the band gaps are included in Table IV. The band gaps here do not include zero-point motion electron-phonon coupling corrections. In Ref. [21] these were estimated to be of the order of  $-0.2$  eV. On the other hand, the overestimate of the volume by about 2% leads to an underestimate of the band gap. Using a band gap deformation potential  $dE_g/d \ln V$  of  $-8.7$  eV [21], the volume correction would increase the gap by about 0.2 eV. Thus, these two corrections nearly cancel each other. For GaN, likewise, our

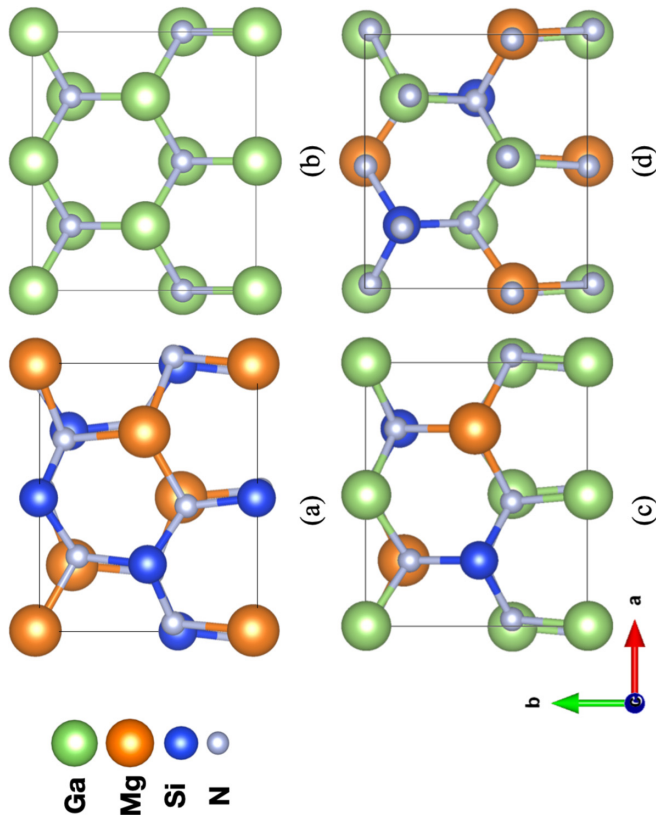


FIG. 1. Octet-rule-preserving MgSiGa<sub>2</sub>N<sub>4</sub> structures in (c) *Pmn*2<sub>1</sub> and (d) *P1n*1 space groups and their relation to the compounds (a) MgSiN<sub>2</sub> and (b) GaN, both in the *Pbn*2<sub>1</sub> structure.

TABLE III. Cohesive energies, energy of formation, and mixing energies in GGA (in eV/atom). The values given in parentheses are obtained using the QE method; the other ones are obtained using QUESTAAL.

	MgSiN <sub>2</sub>	GaN	<i>Pmn</i> 2 <sub>1</sub>	<i>P1n</i> 1
$E_{\text{coh}}$	5.25 (5.31)	4.39 (4.42)	4.82 (4.86)	4.80 (4.84)
$E_{\text{for}}$	-1.19 (-1.19)	-0.52 (-0.47)	-0.90 (-0.83)	-0.88 (-0.81)
$E_{\text{mix}}$			0.008 (0.007)	0.029 (0.031)

TABLE IV. Band gaps of compounds and alloys in various approximations.

Compound	Gap	GGA	$0.8\Sigma$	$0.8\Sigma + \Delta(0)^a$
MgSiN <sub>2</sub>	Indirect	4.03	6.15	5.84
MgSiN <sub>2</sub>	Direct	4.36	6.52	6.28
GaN	Direct	1.72	3.08	
MgSiGa <sub>2</sub> N <sub>4</sub> ( <i>Pmn</i> 2 <sub>1</sub> )	Direct	2.98	4.83	
MgSiGa <sub>2</sub> N <sub>4</sub> ( <i>Pmn</i> 2 <sub>1</sub> )	Indirect	2.92	4.76	
MgSiGa <sub>2</sub> N <sub>4</sub> ( <i>P1n</i> 1)	Direct	2.73	4.60	
MgSiGa <sub>2</sub> N <sub>4</sub> ( <i>P1n</i> 1)	Indirect	2.70	4.57	

<sup>a</sup> $\Delta(0)$  is an estimated zero-point motion correction from Ref. [21].

gap here is underestimated by about 0.2–0.3 eV because of our use of the GGA volume. The band structures are shown in Fig. 2. The overview band structure shows that the top set of valence bands between  $-8$  and  $0$  eV is predominantly N  $2p$ -like, as expected for a nitride. They show projections on the local partial waves. Near the bottom of the valence band we can see that the states bond between N  $2p$  and Si  $s$  and Ga  $s$ . The Mg  $s$  contribution is less strongly present. The conduction band minimum atomic orbital character is more readily seen in the colored bands, which indicate the contribution of the Ga  $s$  muffin-tin-orbital basis functions. The corresponding Si  $s$  and Mg  $s$  are not shown but are significantly smaller. The predominant Ga  $s$  rather than Mg or Si  $s$  character of the CBM is consistent with a quantum well model. *Pmn*2<sub>1</sub> is essentially an ultrathin superlattice of half unit cell GaN quantum wells and half unit cell MgSiN<sub>2</sub> units stacked along the **b** direction. The band offset is type I with a conduction band offset of about 1.4 eV according to Ref. [34], and hence, if the quantum well just captures a single bound state, it could be at about 1.4 eV above the GaN CBM. The quantum confined effects for the holes are expected to be smaller since the effective masses are much larger. The wider the barrier of MgSiN<sub>2</sub> is in this case, the stronger the quantum confinement effects will be, and hence, the larger the gap of the (MgSiN<sub>2</sub>)<sub>*x*</sub>(GaN)<sub>*1-x*</sub> alloys will be.

A close-up near the VBM and CBM for both structures shows that the VBM does not occur at  $\Gamma$  but rather at  $Y$ ,  $(0, \pi/2b, 0)$ , and thus, strictly speaking, we still have an indirect gap system. However, this location of the VBM is different from that of MgSiN<sub>2</sub>, where it occurs at  $U$ ,  $(\pi/2a, 0, \pi/2c)$ , and the energy difference between the VBMs at  $\Gamma$  and  $Y$  here is very small. Furthermore, this is expected to be rather sensitive to strain. It also shows details of the crystal field splitting at  $\Gamma$  in the *Pmn*2<sub>1</sub> structure. The partial density of states in the CBM shows that near the CBM the N  $s$  partial waves dominate over the cation  $s$  states, but we should recall that these are antibonding  $s$  states and that the dominant Ga  $s$  muffin-tin orbital (as shown by the band color) extends into the N spheres and they thus also contribute to the N  $s$  partial density of states.

The bands at  $\Gamma$  were symmetry labeled for *Pmn*2<sub>1</sub>. The point group is  $C_{2v}$ . In this point group,  $\Gamma_1$  (or  $a_1$ ) corresponds to the  $z$  basis function with  $x, y, z$  along  $(a, b, c)$ , respectively,  $\Gamma_2$  corresponds to  $b_2$  or  $y$ , and  $\Gamma_4$  corresponds to  $b_1$  or  $x$ .  $a_2$  or  $\Gamma_3$  corresponds to the  $xy$  basis function. The CBM has  $\Gamma_1$  symmetry and is  $s$ -like. Thus, allowed dipole transitions occur

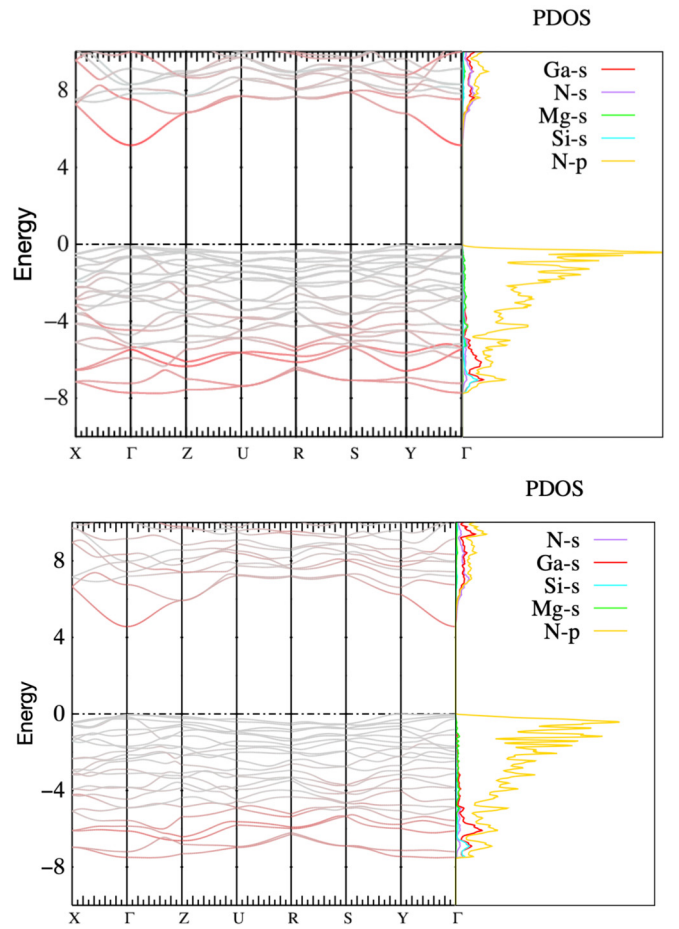


FIG. 2. Band structures and the corresponding partial density of states are shown for both the *Pmn*2<sub>1</sub> (top) and *P1n*1 (bottom) space groups of the MgSiGa<sub>2</sub>N<sub>4</sub> alloy. The band structures are calculated in the  $0.8\Sigma$  approximation, and Ga  $s$  orbitals are color-coded with a red scale, while the rest of the orbitals are in gray scale. In both structures, the VBM is found to be on the  $Y$   $k$  point, but the difference between the VBM and highest valence band energy at  $\Gamma$  is less than 0.1 eV (see Table IV). Partial densities of states (in arbitrary, but consistent, units of states per cell per eV) are given for the orbitals of interest. The valence bands are dominated by the N  $p$  orbitals (gold), while the CBM consists of mostly Ga  $s$  orbitals (red).

between the VBM at  $\Gamma$  and the CBM for  $\mathbf{E} \parallel \mathbf{c}$ . For  $\mathbf{E} \parallel \mathbf{b}$  the transitions occur from the second VBM, and for  $\mathbf{E} \parallel \mathbf{a}$  they occur for the third VBM. The valence band splittings are given in Table V. We also note that the  $z$ -like  $\Gamma_1$  state has the smallest mass along the  $\Gamma$ - $Z$  direction, while the next  $\Gamma_2$  or  $y$ -like state has the smallest mass in the  $\Gamma$ - $Y$  direction and the  $\Gamma_4$  or  $x$ -like

TABLE V. Valence band splittings (in meV) at the  $\Gamma$  point relative to the actual VBM at  $Y$ .

Symmetry	<i>Pmn</i> 2 <sub>1</sub>	Symmetry	<i>P1n</i> 1
$\Gamma_1$	-63	+	-37
$\Gamma_2$	-90	-	-56
$\Gamma_4$	-159	+	-162
		-	-261

TABLE VI. Electron effective masses (in units of free electron mass  $m_e$ ) at  $\Gamma$  for the CBM and top valence bands in close vicinity to the VBM are given for the  $Pmn2_1$  and  $P1n1$  structures. The mass tensor components at the true VBM at  $Y$  are also given. The negative values for valence bands indicate positive hole masses. For the orthorhombic case ( $Pmn2_1$ ), the principal axes are along the crystal axes  $x, y, z$  corresponding to  $a, b, c$ ; for the  $P1n1$  monoclinic space group, one principal axis is along  $y$ , and the others in the  $xz$  plane make an angle  $\alpha_x$  with the  $x$  axis, as indicated.

	CBM	$\Gamma_1$	$\Gamma_4$	$\Gamma_2$	$Y$	
$m_x$	0.244	-3.059	-0.224	-4.321	-0.714	
$m_y$	0.257	-11.302	-3.887	-0.272	-1.105	
$m_z$	0.226	-0.196	-2.567	-2.494	-1.666	
	CBM	$+_1$	$-_1$	$+_2$	$-_2$	$Y$
$m_1$	0.243	-0.286	-0.459	-0.196	-2.372	-0.664
$\alpha_x$	-43.6	2.5	-3.7	91.2	-87.8	0.5
$m_2$	0.240	-2.988	-3.936	-2.652	-2.652	-1.627
$\alpha_x$	46.4	92.5	86.3	1.2	2.2	89.5
$m_3$	0.264	2.167	-0.948	-2.348	-0.251	-3.025

state has its lowest mass in the  $\Gamma$ - $X$  direction. Unfortunately, the top of the VBM is thus  $z$ -like, which implies that the same problem as for Al <sub>$x$</sub> Ga <sub>$1-x$</sub> N occurs at high Al concentration  $x$ . Namely, the lowest energy transition is predominantly TM, which hinders light extraction for a normal exit angle from the basal plane. However, this is sensitive to strain, and the splitting between the  $\Gamma_2$  and  $\Gamma_1$  states is quite small and could, perhaps, more easily be reversed by some strain engineering. Also, it might be possible to grow these materials as films with surfaces other than the basal plane, in which case the  $c$  axis would be in the plane.

For the  $P1n1$  structure, we have only a double-glide mirror plane  $n$  perpendicular to the  $b$  axis, so the point group is  $C_s$ , and states can be labeled only even or odd with respect to the  $n_y$  mirror plane. Obviously,  $y$  orbitals are odd with respect to this mirror plane, while  $x$  and  $z$  are even. We can see some interesting changes in the band structure reflecting the lower symmetry. First, at  $\Gamma$ , there are now four states instead of three within the first 0.3 eV below the VBM. Along the  $\Gamma$ - $X$  line we can see that the top two bands cross, indicating that they have different irreducible representations,  $+$  and  $-$ . The next band down has  $+$  symmetry and therefore an avoided crossing with the  $+$  band emanating from the VBM at  $\Gamma$ . Along  $\Gamma$ - $Y$ , however, there is no symmetry left at all, and hence, the top bands can repel each other, while in  $Pmn2_1$  these bands were allowed to cross because of their different even or odd characters with respect to the  $m_x$  mirror plane.

We have also determined the effective mass tensors at the band edges, as given in Table VI. The curvatures are determined by fitting the bands to a parabolic dispersion very close to the band edge in question in several directions and subsequently determining the principal values and direction of the constant energy surfaces. The conduction band mass tensor shows only slight anisotropy consistent with the point group symmetry. In the  $P1n1$  case, one principal axis is along  $y$ ; the other two can be at some angle from  $x$  in the  $xz$  plane because the point group is only  $C_s$ . For the CBM, we find

these angles are near  $45^\circ$ . The three highest valence bands at  $\Gamma$  show a larger anisotropy, with the smallest negative mass occurring in the direction that corresponds to the irreducible representation of the band in question. In terms of the well-known  $\mathbf{k} \cdot \mathbf{p}$  expression for the inverse effective mass tensor,

$$M_{\alpha\beta}^{-1} = \delta_{\alpha\beta} \frac{1}{m_e} + \frac{1}{m_e^2} \sum_{n' \neq n} \frac{\langle n\mathbf{k} | p_\alpha | n'\mathbf{k} \rangle \langle n'\mathbf{k} | p_\beta | n\mathbf{k} \rangle + \text{c.c.}}{E_{n\mathbf{k}} - E_{n'\mathbf{k}}}, \quad (1)$$

we can see that the interaction of the top valence band with the conduction band would make a small negative contribution to the  $M_{zz}^{-1}$  and no contribution at all for  $M_{xx}^{-1}$  or  $M_{yy}^{-1}$  because only  $p_z$  matrix elements can couple the VBM of  $\Gamma_1$  symmetry to the  $\Gamma_1$  CBM. On the other hand, in the  $x$  ( $y$ ) directions, there are valence band states just below it of symmetry  $\Gamma_4$  ( $\Gamma_2$ ) which will couple to the VBM of  $\Gamma_1$  symmetry and hence cause a large positive change in  $M_{xx}^{-1}$  or  $M_{yy}^{-1}$ . This means a large negative change in the mass itself because  $\Delta(1/m) = -\Delta m/m^2$ . Thus, we find strongly negative masses for the  $x$  and  $y$  directions for the  $\Gamma_1$  VBM. This implies a high positive hole mass in these directions. Other lower-lying  $\Gamma_1$  states will also make a negative contribution to the effective mass in the  $z$  direction, but because these states are farther away, they will result in a smaller negative mass in the  $z$  direction. Similar reasoning explains the other cases. For the  $\Gamma_2$  second valence band, the  $\Gamma_1$  state above it, which is the smallest energy difference, will make a strong negative contribution to  $M_{yy}^{-1}$  in the  $\Gamma$ - $Y$  direction and thus a positive change to the mass itself which must compensate the effect from bands of  $\Gamma_1$  symmetry lying deeper in the valence band. Hence, the smallest mass is along the  $y$  direction for a state with  $\Gamma_2$  or  $y$  symmetry. For the  $P1n1$  case, the top valence band along  $y$  is seen to have a positive curvature because of the strong repulsion of the two valence bands along this symmetry line. For the mass tensor at  $Y$  we can see for  $Pmn2_1$  that  $(m_x m_y m_z)^{1/3} = 1.09$ , so the effectively average density of states mass is close to the free electron mass. For the  $P1n1$  structure the effective density of states mass is 1.48, thus somewhat higher. However, the conduction band masses are similar and again nearly isotropic.

Finally, we estimate the band gap bowing in the alloy system. The band gap is estimated as  $E_g(x) = E_g(0) + xE_g(1) - bx(1-x)$ . For the direct  $\Gamma$ - $\Gamma$  gap we find  $b \approx 0.6$  eV, while for the  $U$ - $\Gamma$  gap it is about 0.7 eV. The results are shown in Fig. 4. They show that a band crossing between direct and indirect gaps still occurs at about  $x = 0.75$  with a gap as high as 5.6 eV at this point. We note that in principle, octet-rule-conserving superlattice-type structures with half unit cells of MgSiN<sub>2</sub> and GaN stacked along the  $b$  direction as building blocks can be designed [17]. However, in a more disordered alloy system, one may expect some octet-rule-violating motifs to exist, in particular those that involve a change in local valence by only  $\pm 1$ . Their presence would likely decrease the gap by creating a tail of defect-related states in the gap near the band edges. From related ternary compounds such as ZnGeN<sub>2</sub> we expect these to reduce the gap by about  $0.5 \pm 0.2$  eV. This would still leave a nearly direct gap larger than 4 eV but with a larger band gap bowing of  $b \approx 2.6$ . In this more disordered system, the distinction between the slightly lower indirect gap

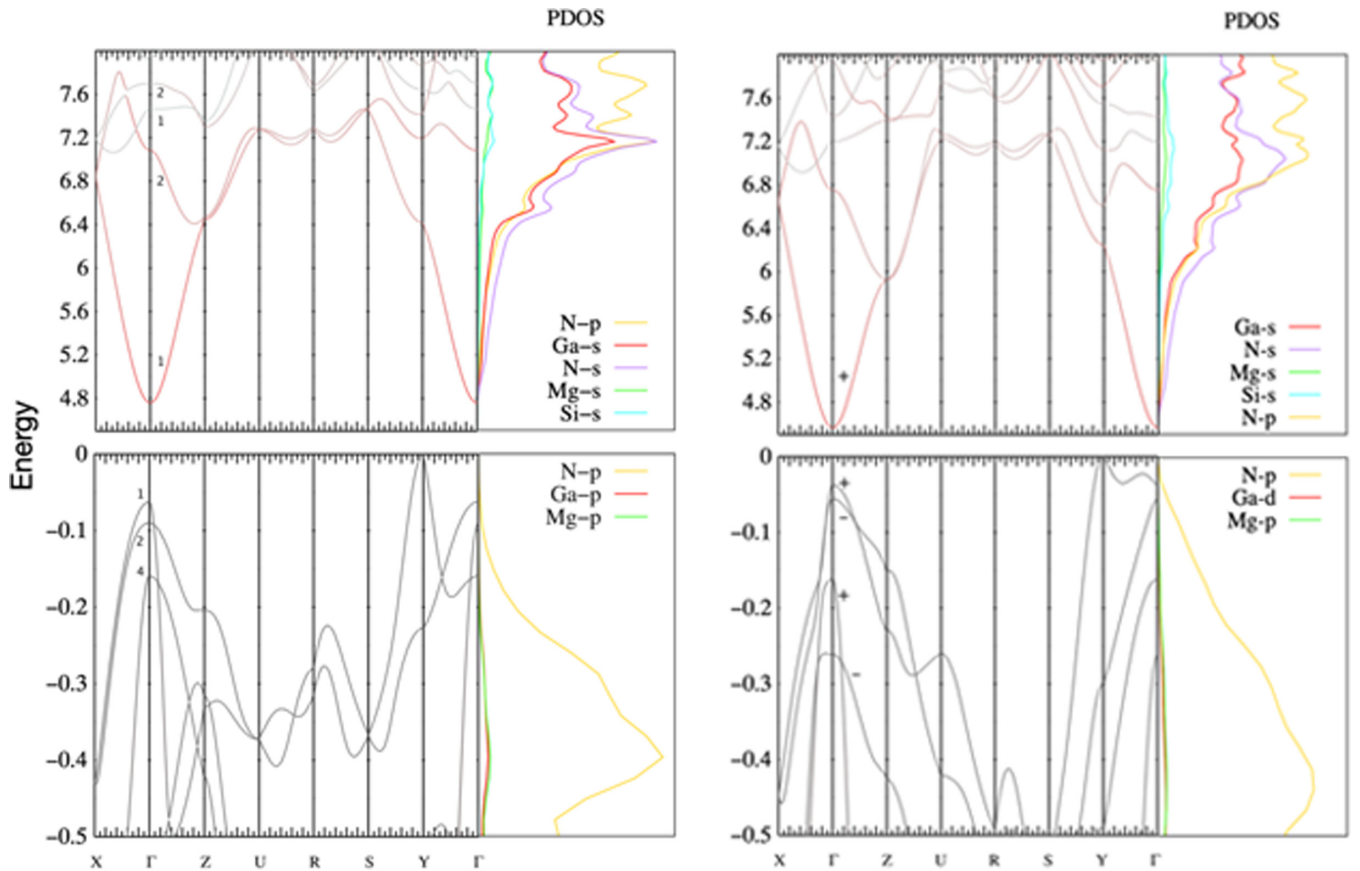


FIG. 3. Band splittings and their symmetries are shown for  $Pmn2_1$  (left) and  $P1n1$  (right) structures, along with the partial density of states of dominant orbitals. The same color coding as in Fig. 2 is used.

$Y-\Gamma$  and the direct gap would be essentially wiped out by the disorder-induced band broadening.

#### IV. CONCLUSIONS

We have shown that a 50% alloy of  $MgSiN_2$  and GaN is promising as an alternative to  $Al_xGa_{1-x}N$  alloys for increas-

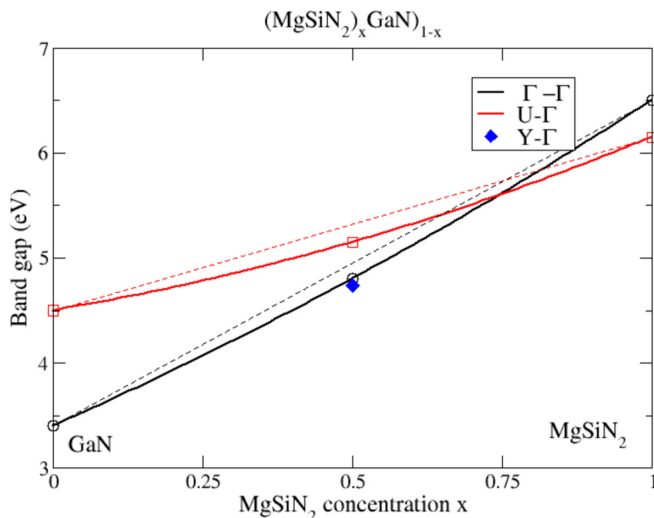


FIG. 4. Band gaps in the  $(MgSiN_2)_x(GaN)_{1-x}$  alloy system.

ing the gap beyond that of GaN to allow for optoelectronic applications into the deep UV region. First, we find that two octet-rule compounds exist with the composition  $MgSiGa_2N_4$  which have negative energies of formation and only a small positive mixing energy with respect to GaN and  $MgSiN_2$ . While we expect octet-rule-violating motifs to increase the mixing energy, we still expect such alloys to be feasible. In its lowest energy structure with space group  $Pmn2_1$ , the lattice constant in the  $a$  direction has only a +0.5% mismatch with the corresponding lattice constant in GaN, and the positive sign indicates that on a GaN substrate this compound would be under compression in this direction. In the other direction in the basal plane, its mismatch is  $-2.3\%$ . The band gap of this structure is nearly direct, by which we mean that the direct gap is less than 0.1 eV below the direct gap at  $\Gamma$ , and the direct gap is calculated to be 4.83 eV. Another structure with space group  $P1n1$  also has a fairly good lattice mismatch with GaN and a nearly direct gap of 4.76 eV. These small deviations from direct gap character could possibly be overcome by strain tuning.

We should point out some caveats here. For a quaternary system, achieving the precise  $Pmn2_1$  ordering is even more challenging than for a ternary, and moving away from the perfect 50% stoichiometry of  $MgSiN_2-(GaN)_2$  would likely introduce even more cation disorder in the form of locally octet-rule-violating motifs. This is expected to decrease the band gap somewhat, but a direct gap larger than 4 eV is still expected. On the other hand, octet-rule-satisfying

TABLE VII. Reduced coordinates of atoms for the  $Pmn2_1$  structure.

Atom	Wyckoff <sup>a</sup>	$x$	$y$	$z$
Ga	4b	0.25162	-0.32950	0.49925
Mg	2a	0.00000	0.16007	0.49196
Si	2a	0.00000	-0.17887	0.00043
N <sub>Ga</sub>	4b	0.22286	-0.32754	0.88188
N <sub>Mg</sub>	2a	0.00000	0.13495	0.90272
N <sub>Si</sub>	2a	0.00000	-0.19564	0.34264

<sup>a</sup>The 2a positions are  $(x, y, z)$  and  $(1/2, -y, z + 1/2)$ , and the 4b positions are  $(x, y, z)$ ,  $(-x + 1/2, -y, z + 1/2)$ ,  $(x + 1/2, -y, z + 1/2)$ , and  $(-x, y, z)$ .

superlattices at different concentrations are, in principle, possible and may provide higher gaps but are even more challenging to achieve. To facilitate comparison with future experimental realizations of these materials, we have provided ample details on their predicted crystal structure and band structure, including the effective mass tensors at the band edges.

#### ACKNOWLEDGMENTS

The calculations were performed on the High Performance Computing Resource in the Core Facility of Advanced

TABLE VIII. Reduced coordinates of atoms for the  $P1n1$  structure.

Atom	Wyckoff <sup>a</sup>	$x$	$y$	$z$
Ga <sub>1</sub>	2a	0.49984	-0.15530	-0.00064
Ga <sub>2</sub>	2a	0.74905	-0.32606	0.49904
Mg	2a	0.25124	-0.33223	0.49367
Si	2a	0.00024	-0.16716	0.00067
N <sub>Ga1</sub>	2a	0.50965	-0.13049	0.38153
N <sub>Ga2</sub>	2a	0.26846	0.30852	0.38142
N <sub>Mg</sub>	2a	0.73140	0.32936	0.40271
N <sub>Si</sub>	2a	-0.00986	-0.16526	0.34159

<sup>a</sup>All atoms are in 2a positions:  $(x, y, z)$ ,  $(-x + 1/2, -y, z + 1/2)$ .

Research Computing at Case Western Reserve University. This work was supported by the U.S. Department of Energy Basic Energy Sciences (DOE-BES) under Grant No. DE-SC0008933.

#### APPENDIX: STRUCTURAL DETAIL

The reduced coordinates of the atoms and their Wyckoff designations are given in Tables VII and VIII for  $Pmn2_1$  and  $P1n1$ , respectively.

- [1] M. Kneissl, T.-Y. Seong, J. Han, and H. Amano, The emergence and prospects of deep-ultraviolet light-emitting diode technologies, *Nat. Photonics* **13**, 233 (2019).
- [2] M. Crawford, Materials challenges of AlGaIn-based UV optoelectronic devices, in *III-Nitride Semiconductor Optoelectronics*, edited by Z. Mi and C. Jagadish, Semiconductors and Semimetals Vol. 96 (Elsevier, Amsterdam, 2017), pp. 3–44.
- [3] T. Detchprohm, X. Li, S.-C. Shen, P. Yoder, and R. Dupuis, III-N wide bandgap deep-ultraviolet lasers and photodetectors, in *III-Nitride Semiconductor Optoelectronics*, edited by Z. Mi and C. Jagadish, Semiconductors and Semimetals Vol. 96 (Elsevier, Amsterdam, 2017), pp. 121–166.
- [4] M. Shatalov, R. Jain, T. Saxena, A. Dobrinsky, and M. Shur, Development of deep UV LEDs and current problems in material and device technology, in *III-Nitride Semiconductor Optoelectronics*, edited by Z. Mi and C. Jagadish, Semiconductors and Semimetals Vol. 96 (Elsevier, Amsterdam, 2017), Chap. 2, pp. 45–83.
- [5] H. Hirayama, Growth of high-quality AlN on sapphire and development of AlGaIn-based deep-ultraviolet light-emitting diodes, in *III-Nitride Semiconductor Optoelectronics*, edited by Z. Mi and C. Jagadish, Semiconductors and Semimetals Vol. 96 (Elsevier, Amsterdam, 2017), Chap. 3, pp. 85–120.
- [6] S. Zhao and Z. Mi, Al(Ga)N nanowire deep ultraviolet optoelectronics, in *III-Nitride Semiconductor Optoelectronics*, edited by Z. Mi and C. Jagadish, Semiconductors and Semimetals Vol. 96 (Elsevier, Amsterdam, 2017), Chap. 5, pp. 167–199.
- [7] J. Zhang, H. Zhao, and N. Tansu, Effect of crystal-field split-off hole and heavy-hole bands crossover on gain characteristics of high Al-content AlGaIn quantum well lasers, *Appl. Phys. Lett.* **97**, 111105 (2010).
- [8] C. Reich, M. Guttmann, M. Feneberg, T. Wernicke, F. Mehnke, C. Kuhn, J. Rass, M. Lapeyrade, S. Einfeldt, A. Knauer, V. Kueller, M. Weyers, R. Goldhahn, and M. Kneissl, Strongly transverse-electric-polarized emission from deep ultraviolet AlGaIn quantum well light emitting diodes, *Appl. Phys. Lett.* **107**, 142101 (2015).
- [9] W. R. L. Lambrecht and A. Punya, Heterovalent ternary II-IV-N<sub>2</sub> compounds: Perspectives for a new class of wide-band-gap nitrides, in *III-Nitride Semiconductors and Their Modern Devices*, edited by B. Gill (Oxford University Press, Oxford, 2013), Chap. 15, pp. 519–585.
- [10] S. Lyu, D. Skachkov, K. Kash, E. W. Blanton, and W. R. L. Lambrecht, Band gaps, band-offsets, disorder, stability region, and point defects in II-IV-n<sub>2</sub> semiconductors, *Phys. Status Solidi A* **216**, 1800875 (2019).
- [11] A. D. Martinez, A. N. Fioretti, E. S. Toberer, and A. C. Tamboli, Synthesis, structure, and optoelectronic properties of II-IV-V<sub>2</sub> materials, *J. Mater. Chem. A* **5**, 11418 (2017).
- [12] P. C. Quayle, E. W. Blanton, A. Punya, G. T. Junno, K. He, L. Han, H. Zhao, J. Shan, W. R. L. Lambrecht, and K. Kash, Charge-neutral disorder and polytypes in heterovalent wurtzite-based ternary semiconductors: The importance of the octet rule, *Phys. Rev. B* **91**, 205207 (2015).
- [13] D. Skachkov, P. C. Quayle, K. Kash, and W. R. L. Lambrecht, Disorder effects on the band structure of ZnGeN<sub>2</sub>: Role of exchange defects, *Phys. Rev. B* **94**, 205201 (2016).
- [14] S. Lany, A. N. Fioretti, P. P. Zawadzki, L. T. Schelhas, E. S. Toberer, A. Zakutayev, and A. C. Tamboli, Monte Carlo simulations of disorder in ZnSnN<sub>2</sub> and the effects on the electronic structure, *Phys. Rev. Mater.* **1**, 035401 (2017).

- [15] J. J. Cordell, G. J. Tucker, A. Tamboli, and S. Lany, Bandgap analysis and carrier localization in cation-disordered ZnGeN<sub>2</sub>, *APL Mater.* **10**, 011112 (2022).
- [16] T. D. Veal, N. Feldberg, N. F. Quackenbush, W. M. Linhart, D. O. Scanlon, L. F. J. Piper, and S. M. Durbin, Band gap dependence on cation disorder in ZnSnN<sub>2</sub> solar absorber, *Adv. Energy Mater.* **5**, 1501462 (2015).
- [17] B. H. D. Jayatunga, S. Lyu, S. K. Radha, K. Kash, and W. R. L. Lambrecht, Ordering in the mixed ZnGeN<sub>2</sub>-GaN alloy system: Crystal structures and band structures of ZnGeGa<sub>2</sub>N<sub>4</sub> from first principles, *Phys. Rev. Mater.* **2**, 114602 (2018).
- [18] B. H. D. Jayatunga, M. R. Karim, R. A. Lalk, O. Ohanaka, W. R. L. Lambrecht, H. Zhao, and K. Kash, Metal-organic chemical vapor deposition of ZnGeGa<sub>2</sub>N<sub>4</sub>, *Cryst. Growth Des.* **20**, 189 (2020).
- [19] T. Suehiro, M. Tansho, and T. Shimizu, Quaternary wurtzitic nitrides in the system ZnGeN<sub>2</sub>-GaN: Powder synthesis, characterization, and potentiality as a photocatalyst, *J. Phys. Chem. C* **121**, 27590 (2017).
- [20] T. Omata, M. Kita, K. Nose, K. Tachibana, and S. Otsuka-Yao-Matsuo, Zn<sub>2</sub>LiGaO<sub>4</sub>, wurtzite-derived wide band gap oxide, *Jpn. J. Appl. Phys.* **50**, 031102 (2011).
- [21] A. P. Jaroenjittichai and W. R. L. Lambrecht, Electronic band structure of Mg-IV-N<sub>2</sub> compounds in the quasiparticle-self-consistent GW approximation, *Phys. Rev. B* **94**, 125201 (2016).
- [22] J. B. Quirk, M. Rålander, C. M. McGilvery, R. Palgrave, and M. A. Moram, Band gap and electronic structure of MgSiN<sub>2</sub>, *Appl. Phys. Lett.* **105**, 112108 (2014).
- [23] J. P. Perdew, K. Burke, and M. Ernzerhof, Generalized Gradient Approximation Made Simple, *Phys. Rev. Lett.* **77**, 3865 (1996).
- [24] P. Giannozzi *et al.*, Quantum Espresso: A modular and open-source software project for quantum simulations of materials, *J. Phys.: Condens. Matter* **21**, 395502 (2009).
- [25] M. van Schilfgaarde, T. Kotani, and S. Faleev, Quasiparticle Self-Consistent GW Theory, *Phys. Rev. Lett.* **96**, 226402 (2006).
- [26] T. Kotani, M. van Schilfgaarde, and S. V. Faleev, Quasiparticle self-consistent GW method: A basis for the independent-particle approximation, *Phys. Rev. B* **76**, 165106 (2007).
- [27] D. Pashov, S. Acharya, W. R. Lambrecht, J. Jackson, K. D. Belashchenko, A. Chantis, F. Jamet, and M. van Schilfgaarde, Questaal: A package of electronic structure methods based on the linear muffin-tin orbital technique, *Comput. Phys. Commun.* **249**, 107065 (2019).
- [28] L. Hedin, New method for calculating the one-particle Green's function with application to the electron-gas problem, *Phys. Rev.* **139**, A796 (1965).
- [29] B. Cunningham, M. Grüning, P. Azarhoosh, D. Pashov, and M. van Schilfgaarde, Effect of ladder diagrams on optical absorption spectra in a quasiparticle self-consistent GW framework, *Phys. Rev. Mater.* **2**, 034603 (2018).
- [30] B. Cunningham, M. Gruening, D. Pashov, and M. van Schilfgaarde, QSGW: Quasiparticle self consistent GW with ladder diagrams in W, [arXiv:2106.05759](https://arxiv.org/abs/2106.05759).
- [31] S. K. Radha, W. R. L. Lambrecht, B. Cunningham, M. Grüning, D. Pashov, and M. van Schilfgaarde, Optical response and band structure of LiCoO<sub>2</sub> including electron-hole interaction effects, *Phys. Rev. B* **104**, 115120 (2021).
- [32] C. Bhandari, M. van Schilfgaarde, T. Kotani, and W. R. L. Lambrecht, All-electron quasiparticle self-consistent GW band structures for SrTiO<sub>3</sub> including lattice polarization corrections in different phases, *Phys. Rev. Mater.* **2**, 013807 (2018).
- [33] D. Deguchi, K. Sato, H. Kino, and T. K. Ni, Accurate energy bands calculated by the hybrid quasiparticle self-consistent GW method implemented in the ecalj package, *Jpn. J. Appl. Phys.* **55**, 051201 (2016).
- [34] S. Lyu and W. R. L. Lambrecht, Band alignment of III-N, ZnO and II-IV-N<sub>2</sub> semiconductors from the electron affinity rule, *J. Phys. D* **53**, 015111 (2020).